Volcanic Ash Cloud Retrieval by Ground-Based Microwave Weather Radar

Frank Silvio Marzano, *Senior Member, IEEE*, Stefano Barbieri, Gianfranco Vulpiani, *Member, IEEE*, and William I. Rose

***Abstract*—The potential of ground-based microwave weather radar systems for volcanic ash cloud detection and quantitative retrieval is evaluated. The relationship between radar reflectivity factor, ash concentration, and fall rate is statistically derived for various eruption regimes and ash sizes by applying a radar-reflectivity microphysical model. To quantitatively evaluate the ash detectability by weather radars, a sensitivity analysis is carried out by simulating synthetic ash clouds and varying ash concentration and size as a function of the range. Radar specifications are taken from typical radar systems at S-, C-, and X-band. A prototype algorithm for volcanic ash radar retrieval (VARR) is discussed. Starting from measured single-polarization reflectivity, the statistical inversion technique to retrieve ash concentration and fall rate is based on two cascade steps, namely: 1) classification of eruption regime and volcanic ash category and 2) estimation of ash concentration and fall rate. Expected accuracy of the VARR algorithm estimates is evaluated using a synthetic data set. An application of the VARR technique is finally shown, taking into consideration the eruption of the Grímsvötn volcano in Iceland on November 2004. Volume scan data from a Doppler C-band radar, which is located at 260 km from the volcano vent, are processed by means of the VARR algorithm. Examples of the achievable VARR products are presented and discussed.**

***Index Terms*—Ash retrieval, inversion methods, microwave radars, volcanic eruption clouds.**

I. Introduction

THE EXPLOSIVE eruptions of active volcanoes with a consequent formation of ash clouds represent a severe threat in several regions of the urbanized world [1]. The injection of large amounts of fine and coarse ash and rock fragments and corrosive gases into the troposphere and lower stratosphere is usually followed by a long-lasting ashfall that can cause a variety of damage [2]–[5]. When volcanic ash accumulates on buildings, its weight can cause roofs to collapse. Because wet ash conducts electricity, it can cause short circuits and failure of electronic components, especially high-voltage circuits and transformers. Eruption clouds and ash fall commonly interrupt or prevent telephone and radio communications in several ways, including physical damage to equipment and frequent lightning due to electrically charged ash particles. Even more important, volcanic ash clouds are an increasing hazard to aviation safety because of growing air traffic volumes that use more efficient and susceptible jet engines [6]. Such explosive eruptions have occurred many times per year across the globe during the past decades [7]. Several hundreds of commercial aircrafts have unexpectedly encountered volcanic ash in flight and at airports in the past 15 years [6]. Tens of these encounters caused in-flight loss of jet engine power, which nearly resulted in the crash of the airplane. A range of damage may occur to airplanes that fly through an eruption cloud, depending on the concentration of volcanic ash and gas aerosols in the cloud, the length of time the aircraft actually spends in the cloud, and the actions taken by the pilots to exit the cloud itself [8]. Fine ash can also be a health hazard as aerodynamically fine particles will be taken into the lungs during breathing.

Real-time and areal monitoring of a volcano eruption, in terms of its intensity and dynamics, is not always possible by conventional visual inspections, especially during worse visibility periods that are quite common during eruption activity. Remote sensing techniques both from ground and from space represent unique tools to be exploited [9], [10]. Satellite multispectral radiometric observations from geostationary satellites are currently used for long-range trajectory tracking, but their observations are available only every 15–30 min and suffer from a relatively poor spatial resolution and possible blockage of ice clouds [11]. Visible and infrared radiometric sensors on near-polar orbiting platforms are also employed to detect and map volcanic ash clouds over the entire globe, even though their temporal repetition, which is usually longer than 12 h (with a single platform), is not compatible with real-time monitoring requirements [12]. Ground-based remote sensors are also utilized to monitor volcano eruptions. Microwave instruments, such as radar wind profilers and global positioning system (GPS) receivers, have been tested [13], [14]. Apart from a specific use, these sensors do not generally have a scanning capability, thus showing a limited spatial coverage. In this respect, microwave weather radars can gather three-dimensional information of atmospheric scattering volumes up several hundreds of kilometers in all weather conditions, at a fairly high spatial resolution (less than a kilometer), and with a repetition cycle of a few minutes [15], [16]. Ground-based radar systems represent one of the best methods for determining the height and volume of volcanic eruption clouds [17], [18].

Manuscript received January 17, 2006; revised April 10, 2006. This work was supported in part by the Italian Ministry of University and Research.

F. S. Marzano and S. Barbieri are with the Department of Electronic Engineering, University of Rome "La Sapienza," 00184 Rome, Italy, and also with the Centro di Eccellenza in Telerilevamento E Modellistica per la Previsione di Eventi Severi (CETEMPS), University of L'Aquila, 67040 L'Aquila, Italy (e-mail: marzano@die.uniroma1.it).

G. Vulpiani is with the Department of Physics and the Centro di Eccellenza in Telerilevamento E Modellistica per la Previsione di Eventi Severi (CETEMPS), University of L'Aquila, 67040 L'Aquila, Italy (e-mail: g.vulpiani@aquila.infn.it).

W. I. Rose is with the Department of Geological Engineering and Sciences, Michigan Technological University, Houghton, MI 49931 USA (e-mail: raman@mtu.edu).

Digital Object Identifier 10.1109/TGRS.2006.879116

Single-polarization Doppler radars can measure horizontally polarized power echo and Doppler shift from which ash content and radial velocity can be, in principle, extracted [19].

In spite of these potentials, there are still several open issues about microwave weather radar capabilities to detect and quantitatively retrieve ash cloud parameters [20]. Several unknowns may diminish the accuracy of radar products, most of them related to microphysical variability of ash clouds due to particle size distribution (PSD), shape, and dielectric composition [21]–[24]. Even though this variability cannot be fully resolved by using the available observables of Doppler weather radars, the accuracy of radar remote sensing of ash clouds can be quantitatively approached by assuming a given uncertainty of the main driving parameters of ash dynamics. In a previous paper, a study on forward model of the ash active remote sensing problem was carried out taking into account various operating frequencies such as S-, C-, X-, and Ka-band [25]. After a summary on evidences of weather radar sensitivity to ash clouds, a microphysical characterization of volcanic ash was defined in terms of quite general modeled PSD functions. The latter have been cast into a scaled Weibull and a scaled Gamma form and parameterized by a best fitting to available ash measurements at ground. The radar backscattering from sphere-equivalent ash particles was simulated up to Ka-band for fine ash, coarse ash, and lapilli. The evaluation of Rayleigh scattering approximation accuracy and a model sensitivity analysis was performed and assessed.

In this paper, to quantitatively evaluate the ash retrieval by weather radars, a prototype algorithm for volcanic ash radar retrieval (VARR) is formulated and discussed in Section II. Starting from measured single-polarization reflectivity, the estimation method has been based on two cascade steps, namely: 1) classification of eruption regime and volcanic ash category and 2) estimation of ash concentration and fall rate. Expected accuracy of the VARR algorithm estimates is evaluated on synthetic data sets in Section III. A minimum detectable reflectivity (MDZ) analysis is accomplished for various ash classes and for some available radar systems at S-, C-, and X-band. Finally, the VARR algorithm is applied to C-band radar data available during the eruption of the Grímsvötn volcano in Iceland in November 2004 in Section V. A discussion on the obtained results together with limitations and potentials of the proposed technique is finally carried out.

II. Volcanic Ash Radar Retrieval

In the following sections, quantitative definitions and a physical parameterization of volcanic ash clouds will be briefly introduced together with some radar reflectivity modeling issues. Note that we will limit our attention to the single-polarization amplitude radar observables. The analysis of dual-polarization and Doppler capabilities for ash cloud retrieval is beyond the scopes of this paper.

A. Volcanic Ash Cloud and Radar Reflectivity Models

Ash particle occurrence per unit volume and unit size can be described by the PSD. A general scaled form has been assumed in this paper to describe ash PSD (measured per millimeter per cubic meter), which is formally expressed by

$$N_a(D) = N_n \left(\frac{D}{D_n}\right)^{\mu} e^{-\Lambda_n \left(\frac{D}{D_n}\right)^{\nu}} \tag{1}$$

where D (in millimeters) is the particle diameter, D_n (in millimeters) is the *number-weighted mean diameter*, and in a logarithmic plane, N_n (measured per millimeter per cubic meter) is the intercept, Λ_n is the slope, μ is the shape factor, and ν is the slope factor. The PSD normalization is such that N_n and Λ_n are related to the mean diameter D_n and ash concentration C_a. The form of (1) is quite general and its derivation is detailed in previous papers [20], [25]. It is demonstrated that (1) may represent both the scaled Weibull PSD (SW-PSD) with $\nu = \mu + 1 = 3\gamma + 3$ and the scaled Gamma PSD (SG-PSD) with $\nu = 1$. In particular, the SW-PSD is shown to be derivable from the Segmentation–Fragmentation Theory, where particle transport and growth are taken into account in a physical manner [26]. The maximum-likelihood best fitting of (1) with respect to available PSD ash measurements has shown that the most probable value of μ is about 1 and 0.5 for a SG-PSD and SW-PSD, respectively [25].

From the knowledge of ash PSD, shape, and composition, some meaningful parameters can be introduced by indicating with m_n the order-n moment of a given PSD [27], [28]. If ρ_a (in grams per cubic meter) is the ash density and $m_a = \rho_a(\pi/6)D^3$ is the mass of sphere-equivalent ash particles, then the *mass concentration* C_a (in grams per cubic meter) can be expressed by

$$C_a \equiv 10^{-3} \int_{D_1}^{D_2} m_a(D) N_a(D) dD = \frac{10^{-3}\pi}{6} \rho_a m_3 \tag{2}$$

where D_1 and D_2 are the minimum and maximum diameter (in millimeters) and m_3 is the third-moment of PSD, whereas the number-weighted mean diameter D_n (in millimeters) is defined by

$$D_n = \frac{\int_{D_1}^{D_2} D N_a(D) dD}{\int_{D_1}^{D_1} N_a(D) dD} = \frac{m_1}{m_0}. \tag{3}$$

The factor 10^{-3} in (2) comes from a dimensional analysis of C_a given in grams per cubic meter. In this paper, we have considered the SW-PSD with $\mu = 3\gamma + 2$ as a reference model. If $D_1 = 0$ and $D_2 = \infty$, the SW-PSD moments of order n are given by

$$m_n = \frac{\left[\Gamma\left(1 + \frac{1}{3(\gamma+1)}\right)\right]^3 \Gamma\left(1 + \frac{n}{3(\gamma+1)}\right)}{\frac{\pi}{6} \cdot \Gamma\left(\frac{\gamma+2}{\gamma+1}\right) \cdot \left[\Gamma\left(1 + \frac{1}{3(\gamma+1)}\right)\right]^n} \frac{D_n^{n-3}}{\rho_a} C_a \tag{4}$$

where Γ is the complete Gamma function and $\gamma = -0.5$ (being $\mu = 0.5$ for SW-PSD).

Ashfall rate R_a (in kilograms per hour per square meter), which is defined as the particle mass crossing a horizontal cross

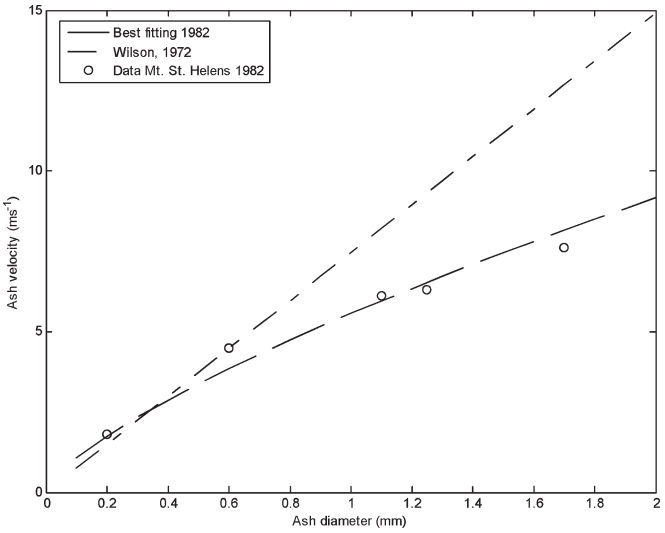

Fig. 1. Best fitting of Harris and Rose's [15] empirical data of ashfall terminal velocity as a function of ash diameter collected at Mt. St. Helens in 1982. Best-fitting curve of Wilson's data [21] is also shown.

section of a unit area over a given interval of time, can be expressed by the following formula:

$$R_a \equiv 3.6 \cdot 10^{-3} \int_{D_2}^{D_1} [v_a(D) - w_{\rm up}]\, m_a(D) N_a(D) dD$$
$$= 3.6 \cdot 10^{-3} \left[\frac{\pi}{6} a_v \rho_a m_{3+b_v} - w_{\rm up} C_a \right] \quad (5)$$

where $v_a(D)$ (in meters per second) is the terminal fall velocity in still air of ash particles, and $w_{\rm up}$ (in meters per second) is the vertical component of the air speed (counted positively upward). The factor $3.6 \cdot 10^{-3}$ in (5) comes out from a dimensional analysis of R_a expressed in kilograms per hour per square meter. The right-hand side of (5) is obtained after assuming a power law for v_a dependence on D, which is expressed as

$$v_a(D) = a_v D^{b_v} \quad (6)$$

where a_v (in meters per second) and b_v are empirical coefficients that can also take into account the correction for the height-dependent air density [21]. Note that the ashfall rate can be also expressed by an equivalent height per unit time through $R_{ah} = R_a/\rho_a$. The estimate of coefficients in (6) is generally done by means of empirical analyses. Fig. 1 shows the best fitting of Harris and Rose's [15] *in situ* data of ashfall terminal velocity as a function of ash diameter, giving $a_v = 5.558\ \mathrm{m \cdot s^{-1}}$ and $b_v = 0.722$ from the year-1982 data of the Mt. St. Helens eruption. Note that from Wilson's data [21], we have obtained $a_v = 7.460\ \mathrm{m \cdot s^{-1}}$ and $b_v = 1.0$ for 5–10 km height, while $a_v = 2.504\ \mathrm{m \cdot s^{-1}}$ and $b_v = 0.472$ from the year-1980 data of the Mt. St. Helens eruption [15].

A previous sensitivity analysis has shown that Rayleigh scattering approximation is well satisfied for radar ash observations up to X-band [25]. Besides, the related specific attenuation is almost always negligible being less than 0.1 dB/km even for intense ash concentration at X-band. If a Rayleigh scattering regime holds, from (1), the horizontally polarized radar reflectivity factor Z_H (in millimeters to the sixth power per cubic meter) is [27]

$$Z_H = \frac{\lambda^4}{\pi^5 |K_a|^2} \eta_H = \int_{D_1}^{D_2} D^6 N_a(D) dD = m_6 \quad (7)$$

where η_H is the radar reflectivity, K_a is the complex dielectric factor, and λ is the radar wavelength. The average value of $|K_a|^2$ is about 0.39 at microwave [25]. The reflectivity factor Z_H is proportional to the sixth power of the particles diameter, and consequently, the larger particles tend to provide a much larger contribution to the reflectivity factor than smaller particles of equal abundance. For brevity, hereinafter, the term radar reflectivity will also stand for radar reflectivity factor.

B. Retrieval of Volcanic Ash From Radar Reflectivity Data

The estimate of volcanic ash concentration from radar measurements can be approached in different ways. A physical approach is to derive an analytical relationship between the radar-observable Z_H within each range bin and ash physical parameters such as its concentration C_a and rate R_a by exploiting the forward analytical model, which is implicitly given in (7). Inserting (4) into (2) and (5) for as SW-PSD with $\mu = 0.5$, it is quite straightforward to obtain

$$\begin{cases} C_a = \left(10^{-3} \frac{\pi \rho_a}{6} \frac{m_3}{m_6}\right) Z_H \cong 3.21 \cdot 10^{-5} \frac{\rho_a}{D_n^3} Z_H \\ R_a = \left(3.6 \cdot 10^{-3} \frac{a_v \pi \rho_a}{6} \frac{m_{3+b_v}}{m_6}\right) Z_H \cong 2.03 \cdot 10^{-4} \frac{a_v \rho_a}{D_n^{3+b_v}} Z_H \end{cases} \quad (8)$$

where the physical dimensions of C_a, R_a, Z_H, v_a, and a_v are those already specified in (2), (3), (5), and (6)—note that the vertical component $w_{\rm up}$ of the air speed has been assumed zero in (5). Previous equations may represent a physical relation to convert radar reflectivity into ash parameters. However, the conversion coefficients are unknown as they depend on ash PSD moments within each radar bin. The relation between Z_H, R_a, and C_a may vary in space and time, and the dependence on ash regimes and size ranges may be relatively significant. Vertical air motion, which is due to local updrafts, and ash vertical gradients rate, which is due to microphysical ash growth and fragmentation, can locally modify PSD behavior.

When using single-polarization weather radars, the inverse problem is substantially ill posed, and to circumvent this difficulty, it can be stated as an estimation problem in a probabilistic framework (e.g., [28]). This means that a probability density, which is derived from available measurements and theoretical knowledge, may be attached to each model-driving parameter. From (1), the driving parameters of ash SW-PSD have been reduced to D_n, C_a, and μ. Indeed, μ (which is related to ν) has been found to be nearly constant and equal to 0.5 for as SW-PSD [20], [25].

To generate physically based random ash classes, we can basically play on D_n and C_a variability. From available literature and ash measurements, we have defined three diameter ash size classes (fine ash, coarse ash, and lapilli) and three

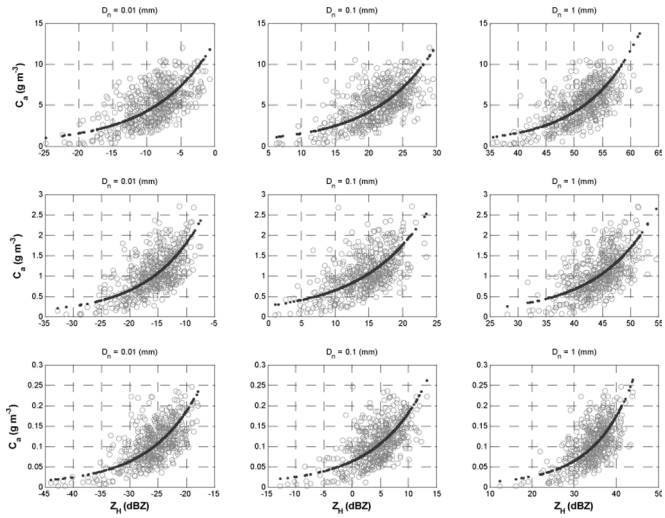

Fig. 2. Statistical relations between C_a and Z_{H_m} for each ash concentration class (i.e., intense, moderate, and light at upper, middle, and lower row panels) and ash size class (i.e., fine ash, coarse ash, and lapilli at left, middle, and right column panels). Regression curves are shown by the dotted line.

concentration regimes (light, moderate, and intense) [11], [15]. As a synthesis of available volcanic information, within each class, we have supposed a Gaussian random distribution for: 1) D_n with average value $\langle D_n \rangle$ equal to 0.01, 0.1, and 1 mm for fine, coarse, and lapilli ash and a standard deviation $\sigma_{D_n} = 0.2\langle D_n \rangle$ and 2) C_a with mean value $\langle C_a \rangle$ equal to 0.1, 1, and 5 g/m^3 for light, moderate, and intense concentration regimes and a standard deviation $\sigma_{C_a} = 0.5\langle C_a \rangle$. The ash density ρ_a has been put equal to an average value of 1 g $\cdot$ cm^{-3} [15].

Fig. 2 depicts the output example of this randomization procedure for the nine ash classes, i.e., $N_c = 9$, which is divided into fine, coarse, and gross sizes and light, moderate, and intense concentrations in terms of C_a versus synthetic measured reflectivity Z_{H_m}. Measured reflectivity factor Z_{H_m} has been obtained from (7), introducing a zero-mean Gaussian random error ε_Z with a given standard deviation σ_Z, which is defined as follows:

$$Z_{H_m} = Z_H + \varepsilon_Z \tag{9}$$

where Z_H is measured in decibels referenced to zero. The error sources may be due to instrumental noise, data processing ambiguities, and modeling uncertainties. An error with a standard deviation σ_Z of 1.4 dBZ has been here assumed due to the following reasoning.

Radar instrumental noise is usually characterized by a standard deviation of 1 dBZ [27]. When dealing with weather radar measurements, other sources of uncertainty should also be taken into account: 1) systematic bias in the radar-measured reflectivity due to miscalibration; 2) attenuation from atmospheric gases, ash particles, and rain depending on frequency and meteorological scenario; 3) partial antenna-beam filling; and 4) ground clutter, anomalous propagation, and multiple-trip echoes. Here, we have supposed that radar data preprocessing has been able to remove these uncertainties. Error modeling can also be included in the error budget. A previous sensitivity analysis has shown that differences of the order of 1 dBZ may

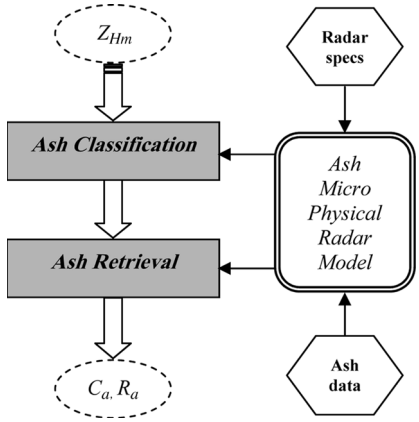

Fig. 3. Schematic block diagram of the VARR algorithm depicting the classification and the retrieval stages, trained by the microphysical radar model parameterized by radar specifications (specs) and ash available data. Z_{H_m} is the measured reflectivity, where C_a and R_a are the ash concentration and fall rate, respectively.

account for reflectivity discrepancies due to the chosen PSD analytical form, ash density, and Rayleigh approximation [25]. If the error sources are statistically independent, the overall error standard deviation of Z_{H_m} in (9) can be assumed to be equal to about $\sqrt{1+1} = 1.4$ dBZ.

Fig. 2 clearly indicates how the proposed nine ash classes can cover a wide range of ash regimes. It is worth mentioning that a given range of reflectivity measurements may be due either to bigger ash particles with a lower concentration or to smaller ash particles with a larger concentration. The nine ash classes show a fairly distinct reflectivity signature even though some residual overlap among the ash classes is also evident.

C. Cascade Statistical Retrieval Methodology

Starting from the previous microphysical–statistical model characterization of ash cloud reflectivity and from given radar specifications, the VARR algorithm has been structured as follows:

1) detection of the ash class from the measured horizontally polarized reflectivity Z_{H_m} within each range bin;
2) retrieval of the ash amount and fall rate from the measured Z_{H_m} by applying one of the statistical relations similar to those derived in Section II-A.

The schematic diagram of VARR is shown in Fig. 3.

1) Classification Step: For what concerns the classification step, its aim is related to the possibility to automatically discriminate between ash categories that were defined as fine, coarse, and lapilli sizes for light, moderate, and intense concentration regimes. In the overall retrieval scheme, classification may represent a first qualitative output before performing parameter estimation. A maximum *a posteriori* (MAP) probability criterion can be used to carry out cloud classification in a model-based supervised context [28], [29]. The MAP approach is framed within the general Bayesian theory and offers the advantage to insert, in a rigorous manner, both the forward modeling and *a priori* information [28]. Besides, using a vector notation, it can be easily extended to a context where multiple observables are available (e.g., Doppler estimate of wind

velocity, polarization diversity measurements, and weather forecast fields) [29].

Using the Bayes theorem, if c is the ash class, then the conditional probability density function (pdf) of a class c given a measurement Z_{H_m} can be expressed as

$$p(c|Z_{H_m}) = \frac{p(Z_{H_m}|c)p(c)}{p(Z_{H_m})} \cong \frac{p(\Delta Z^{(c)})p(c)}{p(Z_{H_m})} \tag{10}$$

where $\Delta Z^{(c)} = Z_{H_m} - m_Z^{(c)}$ (in decibels referenced to zero) is the perturbation of reflectivity measurements from the reflectivity mean value (centroid) $m_Z^{(c)}$ of class c, and $p(c)$ represents the *a priori* discrete pdf of class c. The MAP estimation of ash class c corresponds to the following maximization with respect to c:

$$\hat{c} = \mathrm{Mode}_c \left[\ln\, p(c|Z_{H_m})\right] \tag{11}$$

where Mode_c is the pdf modal value. If $p[\Delta Z^{(c)}]$ is assumed to be a Gaussian pdf, then (11) reduces to

$$\hat{c} = \mathrm{Max}_c \left[-\frac{\left(Z_{H_m} - m_Z^{(c)}\right)^2}{\left(\sigma_Z^{(c)}\right)^2} - \ln\left(\sigma_Z^{(c)}\right)^2 + 2\ln\, p(c) \right] \tag{12}$$

where Max_c is an operator returning the value of c corresponding to its argument maximum and $\sigma_Z^{(c)}$ (in decibels referenced to zero) is the reflectivity standard deviation of class c, whereas the ash classes perturbations have been assumed uncorrelated. Computing (12) requires knowledge of the reflectivity mean $m_Z^{(c)}$ and standard deviation $\sigma_Z^{(c)}$ of each ash class c. This statistical characterization of each cloud class can be derived either from a simulated synthetic data set, as we will do here, or from measured data if available.

The prior pdf $p(c)$ can be used to subjectively weight each class as a function of other available information (such as coincident satellite and/or *in situ* data). From Fig. 2, it is possible to deduce both the mean $m_Z^{(c)}$ and variance $\sigma_Z^{2(c)}$ for the classification into nine classes (all combinations among fine, coarse, and lapilli sizes with light, moderate, and intense ash concentrations).

A simple test of the MAP classification procedure is represented by the results expressed by the contingency matrix, where for each input class, the number of correct and incorrect classifications is counted. Table I reports these results as percentages. For simplicity, we have assumed a uniform *a priori* pdf $p(c)$ in (12). Note that the sum of percentages along a row is always, by construction, equal to 100%, whereas the input classes are those listed along the rows. The classification error budget indicates that, as expected, the fine ash for moderate-to-low concentration regimes are the classes most difficult to detect. On the other hand, the coarse ash and lapilli for intense regimes are quite well distinguished from other classes. Radar sensitivity to each ash class will be analyzed in the next section.

2) Estimation Step: Once an ash class is detected, then an estimate of ash concentration and fall rate is possible. A way to approach the quantitative retrieval problem is to adopt a statistical parametric model to describe the relation $P - Z_{H_m}$, where P stands for either C_a or R_a. Assuming a power-law model, we can write the estimated quantity for each class c as

$$\begin{cases} \hat{C}_a^{(c)} = \alpha[Z_{H_m}]^\beta \\ \hat{R}_a^{(c)} = \gamma[Z_{H_m}]^\delta \end{cases} \tag{13}$$

where $c = 1 : N_c$, and the "hat" indicates estimated quantity. For the nine ash classes and C_a and R_a estimation, Table II shows the root mean square value s_ε and correlation coefficient r_ε of the error ε, which are defined for P as

$$\begin{aligned} s_\varepsilon &= \sqrt{\langle \varepsilon^2 \rangle} = \sqrt{\left\langle (\hat{P} - P)^2 \right\rangle} \\ r_\varepsilon &= \frac{\left\langle \left(\hat{P} - \langle P \rangle\right)(P - \langle P \rangle) \right\rangle}{\sigma_{\hat{P}} \sigma_P} \end{aligned} \tag{14}$$

where the angle brackets stand for ensemble averaging, and σ is the standard deviation. The optimal value of s_ε and r_ε are, of course, 0 and 1, respectively. The error bias has not been evaluated, this test being on synthetic data, and in any case, removable *ex post*. The regression curves for each class are shown in Fig. 2.

The overall average value of the error correlation is about 0.6. It is worth mentioning that the power exponent β and δ in (13) are not equal to 1 as it is derived from the deterministic physical relationships in (8). Their average value is between 0.45 and

TABLE I
CONTINGENCY ERROR TABLE, EXPRESSED IN PERCENTAGE, FOR THE NINE ASH SIZE CATEGORIES

Conc./Size CLASS	*Light /Fine*	*Light / Coarse*	*Light / Lapilli*	*Mod/ Fine*	*Moderate /Coarse*	*Mod /Lapilli*	*Intense /Fine*	*Intense /Coarse*	*Intense /Lapilli*
Light / Fine	93	7	0	0	0	0	0	0	0
Light / Coarse	10.4	70.8	18.8	0	0	0	0	0	0
Light /Lapilli	0.8	13	83	3.2	0	0	0	0	0
Moderate / Fine	0	0.6	6	87	6.4	0	0	0	0
Moderate / Coarse	0	0	0.2	10.2	74.6	15	0	0	0
Moderate / Lapilli	0	0	0	0.8	14.2	82.8	2.2	0	0
Intense / Fine	0	0	0	0	0.4	5.4	87	7.2	0
Intense / Coarse	0	0	0	0	0	0	11.8	71.2	17
Intense / Lapilli	0	0	0	0	0	0	0.8	16.4	82.8

TABLE II
ERROR BUDGET FOR $C_a - Z_{H_m}$ AND $R_a - Z_{H_m}$ ESTIMATION IN TERMS OF ROOT MEAN SQUARE ERROR (IN GRAMS PER CUBIC METER AND KILOGRAMS PER SQUARE METER PER HOUR, RESPECTIVELY) AND CORRELATION COEFFICIENT FOR EACH ASH CLASS

Estimation C_a-Z_{Hm}	**Fine Ash**		**Coarse Ash**		**Lapilli**	
	s_ε	r_ε	s_ε	r_ε	s_ε	r_ε
Light	0.0420	0.53	0.0414	0.56	0.0396	0,60
Moderate	0.3805	0.65	0.3842	0.65	0.3746	0,66
Intense	1.889	0.58	1.8975	0.58	1.7745	0,64
Estimation R_a-Z_{Hm}	**Fine Ash**		**Coarse Ash**		**Lapilli**	
	s_ε	r_ε	s_ε	r_ε	s_ε	r_ε
Light	0.0424	0.58	0.4165	0.59	1.9971	0.60
Moderate	0.0411	0.61	0.3894	0.63	2.0124	0.59
Intense	0.0413	0.60	0.4045	0.60	2.0212	0.58

TABLE III
EXPECTED OVERALL ERROR BIAS, ROOT MEAN SQUARE ERROR, AND CORRELATION ERROR OF THE VARR ALGORITHM FOR ASH CONCENTRATION RETRIEVAL IN TWO CONFIGURATIONS

VARR ALGORITHM	s_ε	r_ε
VARR two-steps (N_c=9)	1.0933	0.9105
VARR one-step (N_c=1)	2.4923	0.25035

0.55 and between 0.55 and 0.65 for C_a and R_a, respectively. This result is due to the aforementioned probabilistic approach, where D_n, which appears in (8) to the third power, has been supposed a Gaussian random variable. It is worth mentioning that the results obtained by looking for a direct relation $Z_{H_m} - C_a$ and then inverting it to estimate C_a, as usually done in radar meteorology practice, instead of searching for the inverse $C_a - Z_{H_m}$ as in (13), would give different results with an increase of s_ε larger than 50%. These results are applicable to S- and C-band, but they may be questionable at X-band, where Mie effects may be not negligible for lapilli with large concentration [20].

III. APPLICATION TO SYNTHETIC DATA

The aim of this section is to discuss the expected performance and the applicability range of the VARR algorithm, shown in Fig. 3 and expressed by the cascade of (12) and (13), using synthetic data. We will first illustrate a numerical evaluation of the overall error budget and then evaluate the minimum detectable amplitude signal for various synthetic eruption scenarios and radar configurations at S-, C-, and X-band.

A. Tests on Classification and Estimate of Volcanic Ash

It is worth noting that the overall error budget is given by the multiplication of the classification error by the estimation error within each class. To ensure a trial on independent data, we have generated a new simulated data set independent from the training data set where both Tables I and II are derived from. For brevity, only tests for ash concentration will be discussed, being those for ashfall rate very similar.

Table III summarizes the results obtained by assuming again an additive Gaussian error on Rayleigh reflectivity measurements of 1.4 dB. It also provides a comparison of the results obtained by using only one ash class, including the overall variability of all nine ash classes given in Fig. 1. In this case, the VARR algorithm collapses into a single step consisting of (13) with $c = 1$ and $N_c = 1$.

The advantage to resort to a cascade two-step algorithm with respect to a single-step approach is clear. In a way, the classification step is a way to perform a stepwise regression to approximate the nonlinear relation between ash concentration and radar reflectivity.

B. Minimum Detectable Reflectivity of Ash Clouds

The application of VARR algorithm to radar data is conditioned to a sufficient level of signal-to-noise ratio due to the observed ash range bin. To this aim, we can use the radar equation that relates the transmitted power to the received power once the radar parameters and medium properties and backscattering response are known. For a single horizontal polarization, the radar equation can be formulated as [27]

$$P_{rH}(r) = P_t |K_a|^2 \frac{\pi^5 10^{-19}}{2^{10} \cdot 1.08 \cdot \ln 2} \frac{\tau \theta_3 \phi_3 G_0^2 L_f}{\lambda^2} \frac{Z_{H_m}(r)}{r^2} \quad (15)$$

where $P_{rH}(r)$ is the received power at H polarization (in milliwatts), r is the range or distance to the scattering volume (in kilometers), P_t is the peak transmitted power (in watts), K_a is the complex dielectric factor for ash particles, τ is the pulse length (in microseconds), ϕ_3 and θ_3 are the horizontal and vertical beamwidths, respectively, to the -3 dB level for a one-way transmission (in degrees), G_0 is the antenna gain along the beam axis, λ is the wavelength (in centimeters), L_r is the receiver filtering loss factor, and Z_{H_m} is the measured reflectivity (in mm^6 per cubic meter). The path attenuation factor at H polarization has been put equal to 1 with the ash absorption negligible up to X-band [25]. Note that $|K_a|^2 \cong 0.39$ for solid ash; by comparison at the same wavelength, this factor is 0.93 for water and 0.197 for ice so that ash reflectivity is 2.4 smaller than that due to liquid water and two times larger than that of ice, having identical PSD and density [20]. The MDZ for a specified scattering volume (i.e., at a given range r) can be evaluated from (15) by assuming a mean received power equal to the minimum detectable signal (MDS), which is defined by

$$\mathrm{MDZ}(r) = \frac{2^{10} \cdot 1.08 \cdot \ln 2}{\pi^5 10^{-19}} \frac{\lambda^2}{\tau \theta_3 \phi_3 G_0^2 |K|^2 L_f P_t} r^2 \mathrm{MDS}. \quad (16)$$

Note that (16) takes into account the noise figure of the radar receiver through MDS (in milliwats or decibels below 1 mW). MDS is generally an available characteristic of a microwave radar system and may assume different values for a specific radar system. Table IV resumes selected characteristics for S-, C-, and X-band radar systems.

These specifications are fairly close to available operational weather radars and to state-of-the-art radar technology at S- and C-band (e.g., [27]). X-band specifications are derived from National Institute for Earth Science and Disaster Prevention polarimetric radar used in the monitoring of the volcano island of Miyake in Japan [17]. It has to be noted that the X-band radar exhibits a lower peak power and antenna gain due to the usual choice to deploy an X-band radar as a portable tool for short- to medium-range applications.

In our simulation environment, a Gaussian-shaped range profile of volcanic ash concentration $C_a(r)$ has been generated. The radar site has been located in the origin of the system coordinate, and the volcanic ash cloud peak has been assumed at a distance d between 30 and 300 km, depending on the pulse repetition frequency (PRF)—note that for PRF $= 250$ Hz, the maximum range $r_{\max} = 600$ km, whereas for PRF $= 2500$ Hz, it results $r_{\max} = 60$ km. The radial resolution has been assumed equal to 300 m (i.e., $\tau = 2$ μs). A range extension (i.e., standard deviation of the ash Gaussian shape) of 20% of the peak distance has been assumed for every synthetic ash cloud together

TABLE IV
THREE DIFFERENT RADAR SYSTEMS AT S-, C-, AND X-BAND AND THEIR TECHNICAL CHARACTERISTICS

RADAR SYSTEM CHARACTERISTICS	*Radar S band*	*Radar C-band*	*Radar X-band*
Band	S	C	X
Frequency Range	2.70 – 2.90 GHz	5.45 – 5.82 GHz	9.375 GHz
Transmitter	Magnetron	Magnetron	Magnetron
Transmit Peak Power	600 Kw	250 kW	50 kW
RF Pulse Width	0.8 to 2 μs	0.5 to 2 μs	0.5 to 2.0 μs
PRF	250 – 5000 Hz	250 – 2500 Hz	250 – 2500 Hz
Antenna Type	Circ. Parabola	Circ. Parabola	Circ. Parabola
Antenna Gain	45 dB	45 dB	41.6 dB
Polarization	Linear H	Linear H	H and V
Half-power Beamwidth	1.0 degree	1.0 degree	1.3 degrees
Reflector diameter	8.5 meters	4.2 meters	2.1 meters
Sensitivity (MDS)	-113 dBm	-113 dBm	-112 dBm
Receiver Noise Figure	2 dB	2 dB	2.3 dB

with a C_a random variation having a standard deviation equal to 10% of the maximum value of the ash profile to generate concentration range gradients. The choice of a Gaussian-shaped range profile is quite arbitrary, but it is aimed to reproduce scenarios where the ash content decreases from the volcano vent either along a downwind or upwind direction, increasing its extension as the ash cloud is advected far from the volcano vent.

The peak concentration of each ash cloud has been set up to reproduce the average values of light, moderate, and intense concentration classes of Fig. 2 and distinguish between fine ash, coarse ash, and lapilli. In practice, we have synthetically generated 36 Gaussian-shaped profiles as a product of all nine ash cloud average classes, which are defined by their centroids $\langle C_a \rangle$ and $\langle D_n \rangle$, and four distances of volcano vent at 30, 60, 120, and 240 km from the radar (see also Section II-B). From a known $C_a(r)$, we have then generated a measured profile $Z_{H_m}(r)$ through (7)–(9) to be compared with the corresponding MDZ(r) for a given radar system. At all considered frequency bands, Rayleigh scattering conditions have been assumed, and this implies that Z_{H_m} is equal for all the bands.

An example of these synthetic ash cloud range profiles is illustrated in Figs. 4 and 5, where the eruption cloud with a peak at 60 km for all nine ash average classes is sketched in terms of comparison between the simulated ash-reflectivity response and the MDZ for the considered radar systems in Table IV at C- and X-band.

The following conclusions can be drawn from this MDZ analysis: 1) For a C-band system, the detection of a fine-ash signal larger than MDZ seems to be possible only in case of very *intense* concentration. On the contrary, for *coarse* and *gross ash*, the radar is able to detect ash particles with reflectivity value larger than zero. 2) For an X-band radar, there is a lower sensitivity to ash content, fine-ash being never detected, and coarse detected only due to a moderate concentration regime.

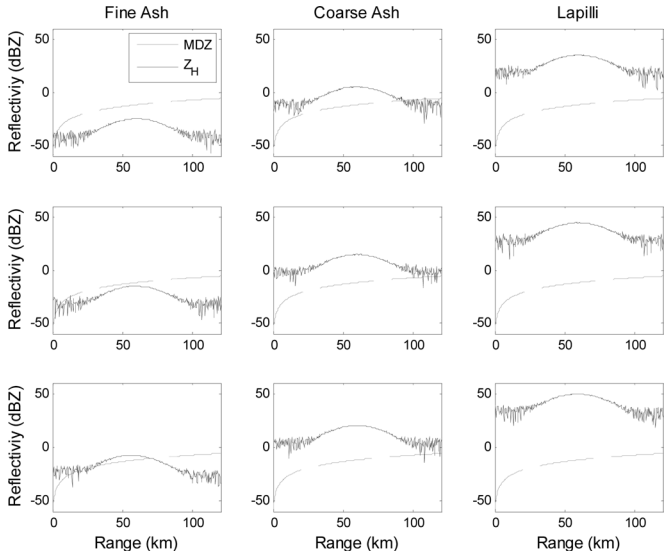

Fig. 4. Reflectivity response and MDZ for ash cloud range profiles with a concentration peak at 60 km at C-band for (top row) a light, (middle row) moderate, and (bottom row) intense concentration and (left) fine, (middle) coarse, and (right) lapilli ash size classes.

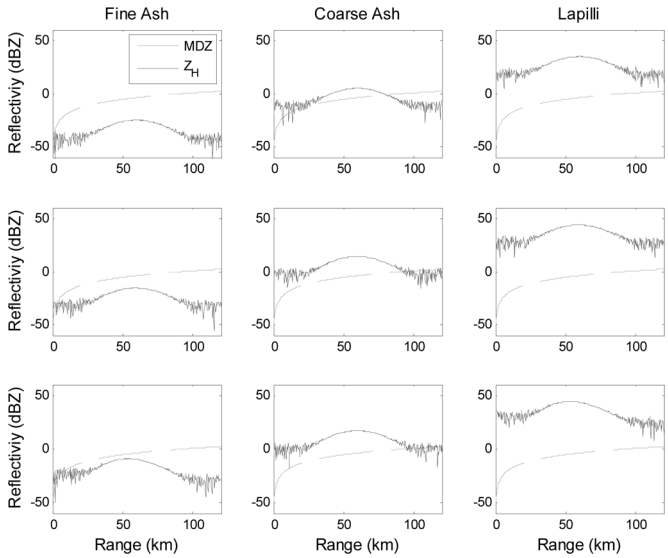

Fig. 5. Same as in Fig. 4, but at X-band.

The chosen X-band system is evidently penalized by characteristics worse than the other two radars (see Table IV). 3) For simulations at S-band, results are slightly worse than at C-band and intermediate with respect to X-band. 4) From results with ash cloud peaks at 30, 120, and 240 km, the increase of the range between the radar and ash cloud (from 30 to 240 km) obviously leads to a worse ash sensitivity of microwave radar response.

Previous intercomparison among S-, C-, and X-band can also be justified by looking at (16) and considering that in the Rayleigh scattering regime, the radar reflectivity is independent of wavelength. For the same radial resolution (or impulse length τ), MDS, and antenna beamwidth, MDZ is proportional to $(\lambda^2 r^2)/G_0 P_t$. Thus, at a given distance r, the S-band system has the advantage of a high P_t contrasted by a larger λ. With respect to S-band, the considered X-band system has a lower

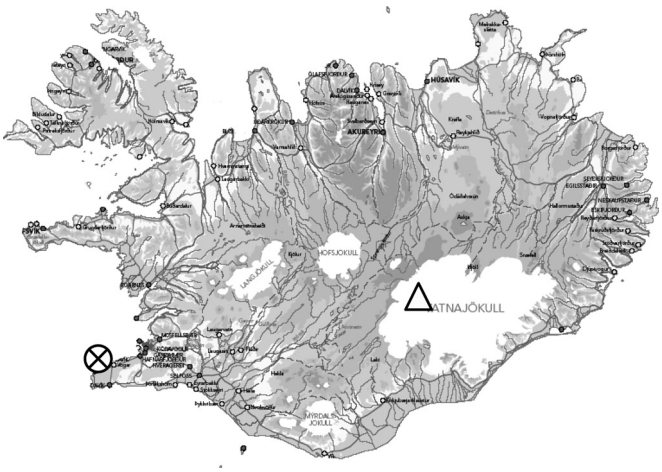

Fig. 6. Location of the Keflavik radar (crossed circle) and the Grímsvötn volcano (triangle) within the Vatnajökull ice sheet, mapped on the topography of Iceland.

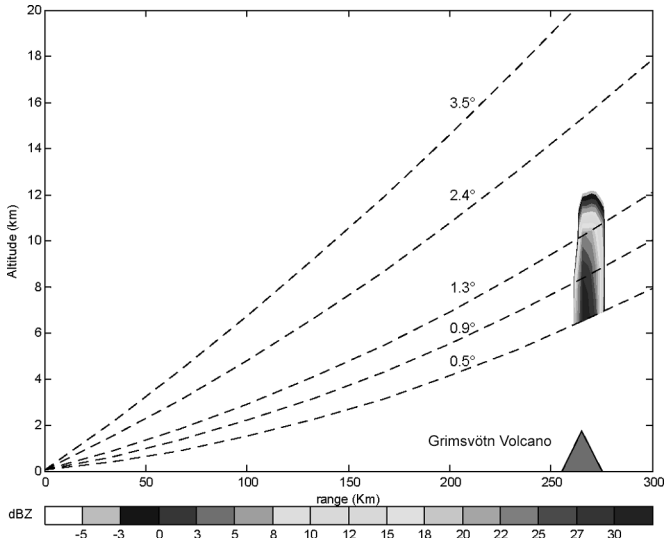

Fig. 7. RHI of the measured horizontally polarized reflectivity (in decibels referenced to zero) along the radar-vent cross section during the Grímsvötn volcano eruption on November 2, 2004, at 04:00 UTM. Reflectivity data are calibrated with a water dielectric factor (i.e., $|K|^2 = 0.93$). Range–height diagram is superimposed as a function of distance between the Keflavik radar and Grímsvötn volcano (schematically indicated by a filled triangle) with elevation angles between 0.5° and 3.5°.

antenna gain (i.e., MDZ increase of about 3.4 dB), a λ that is three times smaller (i.e., MDZ decrease of 9.5 dB for λ^2), an MDS slightly lower than S-band of 1 dBm, and a P_t that is 12 times smaller (i.e., MDZ increase of 10.8 dB).

In conclusion, the specific X-band system is expected to have an MDZ worse than S-band with a loss of about 5.7 dB. On the contrary, following the same argumentation, the C-band system shows a better MDZ than S-band with an overall improvement of 2.2 dBZ. From (16), it is also straightforward to realize that, for a given system, results of Figs. 4 and 5 can be extrapolated to other distances considering that a distance doubling translates into an increase of MDZ of 6 dB. This means that at 240 km and for a C-band radar system, fine ash would no longer be detectable, and coarse ash with low concentration would show a relatively weak radar response. Of course, halving the distance, MDZ is decreased by 6 dB, and by radially averaging reflectivity data, MDZ decreases because the received power is proportional to τ [see (15)].

IV. Application to Measured Data

In the last decade, earthquake activity has increased in the Grímsvötn area in the southeastern region of Iceland [30], [31]. An eruption started in Grímsvötn in the evening of November 1, 2004, and was observed by a C-band weather radar located in Keflavik, Iceland [32]. The aim of this section is to show an application of VARR to experimental data, but the complete analysis of the volcanic eruption is beyond the scope of this paper.

A. C-Band Weather Radar in Keflavik, Iceland

The Keflavik weather radar is an Ericsson C-band radar without a Doppler capability [18]. It is located about 3 km north of the Keflavik International Airport at 47 m above sea level in southwest Iceland, as shown in Fig. 6. It has been in operation since January 1991 for monitoring cloud cover and precipitation. Its main operational characteristics are: transmitted peak power P_t of 245.2 kW, antenna beamwidth of 0.9°, pulse duration τ of 2.15 μm, PRF of 250 Hz, and antenna gain of 44.9 dB.

The radar system at Keflavik is remotely operated by the Icelandic Meteorological Office in Reykjavik, and it has been recently updated. Currently, scanned images are routinely acquired every 20 min for normal weather monitoring and every 5 min during volcanic eruptions. The lowest detectable height by weather radar is a function of the elevation angle of the radar beam, the distance of the target from the radar and the Earth's curvature. Using the Keflavik radar characteristics, this relation can be used to infer the lower and upper radar detection limits above the Grímsvötn volcano.

The range–height ray diagram in a standard atmosphere, which is illustrated in Fig. 7, shows that, based on the distance of about 260 km between the Keflavik radar (64°01′35″ N, 22°38′09″ W) and the Grímsvötn volcano (64°42′ N,17°33′ W), volcanic ash clouds can be detected at heights higher than about 6 km using the minimum elevation of 0.5°. This means that the volcanic eruption cloud cannot be detected between the Grímsvötn summit at 1725 and 6000 m altitude.

B. Grímsvötn Volcano Eruption

Iceland seismic structure is of relevant importance for Icelandic volcanic plume evolution [5]. Since midyear 2003, earthquake activity has increased in the Grímsvötn area [32]. From mid-August 2004, tremor bursts (about 30 min in duration) have been observed at the station of Grímsfjall. On October 28, the seismic records from Kálfafell, south of the Vatnajökull ice sheet, showed signs that a jökulhlaup (i.e., a glacial burst flood) was imminent. The jökulhlaup began early on October 30, and the water level of Skeiðará river began to rise [32]. On the morning of November 1, a jökulhlaup tremor was observed

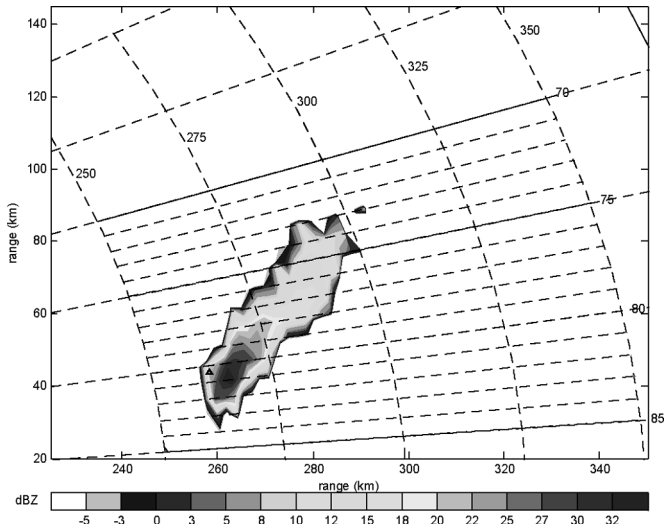

Fig. 8. PPI at 0.5° elevation of the measured horizontally polarized reflectivity at 04:00 UTM during the Grímsvötn volcano eruption on November 2, 2004. The triangle indicates the volcano vent. Reflectivity data are calibrated with a water dielectric factor (i.e., $|K|^2 = 0.93$).

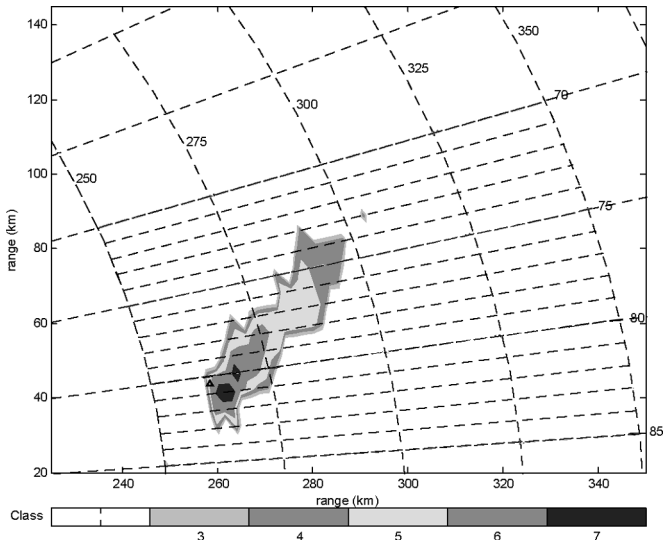

Fig. 9. PPI at 0.5° elevation of the estimated class index c, which was derived from the PPI scan shown in Fig. 8 by applying the VARR classification algorithm. Classes are enumerated as follows: $3 =$ (intense concentration of fine ash); $4 =$ (light concentration of coarse ash); $5 =$ (moderate concentration of coarse ash); $6 =$ (intense concentration of coarse ash); and $7 =$ (light concentration of lapilli). The triangle indicates the volcano vent.

on the seismic records at the Grímsfjall station. In the early morning of November 1, an earthquake swarm began beneath Grímsvötn, and at 20:10, earthquake magnitudes increased, and the swarm intensified. An eruption warning was sent to the Civil Defence at 20:10, November 1. During the next 2 h, about 160 earthquakes were recorded with magnitudes of up to 2.8. Volcanic tremor was first observed, and then an earthquake with a magnitude of 2.7 occurred at 21:50. The frequency of the tremor energy was concentrated at around 1 Hz. The intensity of the tremor increased in the next hours. The volcanic tremor was continuous throughout the night. An increase in power between 04:00 and 05:00 on November 2, 2004 was observed.

Radar volume scans were continuously acquired, and data have been made available from 23:00 on November 1, 2004, to 06:00 on November 2, 2004, every half an hour [32]. Reflectivity data were radially averaged to 2 km. This implies that, since the Keflavik C-band radar has characteristics similar to those in Table IV, from (16), MDZ is about 12 dB larger than that of Fig. 4 due to the four-times longer distance, but it is also about 8 dB smaller due to the equivalent increase of τ from 2.15 to 13.3 μs. This means that the radar sensitivity of the Keflavik radar is not very different from that discussed in Fig. 4.

From available radar imagery, it was observed that the eruption plume increased in size at around 04:00. For the latter time, Fig. 7 displays the range–height indicator (RHI) of the volume scan measurement along a vertical cross section passing through the radar and the volcano vent. All ground clutter echoes and precipitation signatures below 3 km have been properly canceled. Fig. 8 shows the plan position indicator (PPI) radar image at 0.5° elevation angle of the measured reflectivity field at the same time. The image is zoomed, for clarity, around the volcano vent placed at a location around 255 km on x and 42 km on y.

The signal of volcanic cloud is quite evident from both PPI and RHI signatures with values up to 35 dBZ. Notice that the height of this signature avoids any misinterpretation as a rain cloud radar echo, whereas the MDZ of the Keflavik radar at 260 km is about -5 dBZ from (16). At the time of observation after about 5 h from the first radar ash echo, the volcanic plume has been already advected toward the northwest, and the reflectivity maximum contour results to be slightly misplaced with respect to the volcano vent (indicated by a triangle). The extension of the ash cloud area is about 1000 km^2 with an average wind velocity of about 10 km/h.

The measured reflectivity images can then be inverted to retrieve the ash concentration and ashfall rate by applying the VARR technique, which is described in Section II. As noted elsewhere [25], it is worth mentioning that all meteorological radars are operationally calibrated with the dielectric factor K of water, i.e., from (16) $|K_w|^2 = 0.93$ in $Z_{H_m} = (P_{rH} r^2)/(C_r |K_w|^2)$, where C_r is the radar instrumental constant. From (7), we know that the equivalent reflectivity factor of ash particles is given by $Z_H = \eta_H(\lambda^4/(|K_a|^2\pi^5))$. This means that we need to rescale our Rayleigh scattering simulations of Z_H into water-equivalent reflectivity factor Z_{H_w} through $Z_{H_w} = Z_H + 3.77$ (in decibels referenced to zero) since $|K_w|^2/|K_a|^2 = 2.38$.

If the VARR classification algorithm given in (12) is applied, from radar PPI data, we can detect the class index displayed in Fig. 9. The code of the ash classes is listed in the caption of the figure itself. We note that the reflectivity peak is associated to a light concentration of lapilli, which corresponds, from Fig. 2, to an average reflectivity of 34 dBZ. Surrounding this area and closer to the volcano vent, we note the presence of an intense concentration of coarse ash whose average reflectivity is about 21 dBZ. Around this high-reflectivity plume along the northwest direction, there is a dispersion of moderate and light concentrations of coarse ash corresponding to an average reflectivity of 14 and 4 dBZ, respectively. Fine ash is only weakly detected at the border of the PPI sector. This ash areal distribution is quite realistic as the eruption has started a few

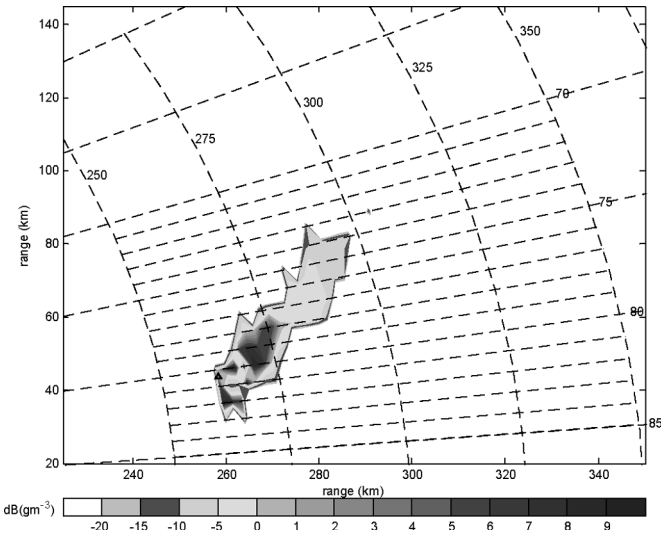

Fig. 10. PPI at 0.5° elevation of the estimated ash concentration C_a (expressed in decibels or 10 $\log_{10}$ grams per cubic meter), which was derived from the PPI scan shown in Fig. 8 by applying the VARR algorithm. The triangle indicates the volcano vent.

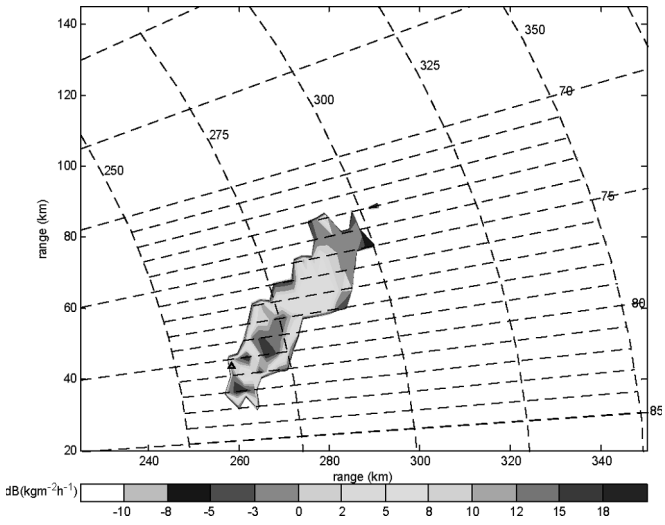

Fig. 11. Same as in Fig. 10, but for the estimated ashfall rate R_a (expressed in decibels or 10 $\log_{10}$ kilograms per square meter per hour).

hours before, and there is experimental evidence that lapilli can be suspended in air for some hours after the explosion [28]. A sorting of ash particles is also typical during the evolution of the erupted volcanic cloud [23]. Unfortunately, we do not have any chance to verify these results within the ash plume.

Fig. 10 shows the results in terms of estimated ash concentration C_a, which is obtained by applying the VARR technique given in (13) to the measured reflectivity PPI data. Analogously, Fig. 11 shows the PPI representation of the estimated ashfall rate R_a. Values of C_a up to 6 $\mathrm{g \cdot m^{-3}}$ and of C_a up to 31 $\mathrm{kg \cdot h^{-1} \cdot m^{-2}}$ are noted. It is worth underlining that the C_a and R_a estimated pattern does not resemble the measured Z_H PPI pattern in the sense that we would have expected the larger concentration in correspondence of higher reflectivity values. This difference may be explained by looking at Fig. 10, taking into account the estimated ash class pattern of Fig. 9. In fact, higher values of radar reflectivity are associated to a low concentration of lapilli. This means that, to give a comparable radar reflectivity, the concentration of coarse ash must be much larger than that of lapilli (see also Fig. 2).

The lack of *in situ* ground data unfortunately prevents the validation of these radar-retrieved maps of ash amount. Some considerations on the retrieved ash map may clarify some current limits of the proposed VARR approach. We have assumed within the radar microphysical forward model that ash clouds are made by solid ash or at most a mixture of air and ash [25]. Ash aggregates, which are made by a mixture of ash with ice and liquid water, have been disregarded [24]. In the case of the Grímsvötn eruption during the fall season, it may happen that ash nucleates ice early in ash cloud history, i.e., right after emplacement high in the atmosphere because magmatic water plus entrained lower tropospheric water is carried upward, thus condensing and freezing. In some ash clouds, this ice rapidly sublimates and disappears in a few hours. However, early in ash clouds the times when coarse ash is present, there is likely to be a lot of ice so that the radar signal may be probably offset by ice growth [18]. However, ice radar reflectivity is at least 3 dB less than that of ash, which should dominate the overall microwave echo. Until we have other radar measurables other than Z_H, such as polarimetric observables, either available *in situ* information or coincident satellite retrieval to discriminate the presence of ice, we cannot assess the effect of ice contamination on ash remote sensing.

V. Conclusion

The potential of using ground-based weather radar systems for volcanic ash cloud detection and quantitative retrieval has been evaluated. The relationship between radar reflectivity factor, ash concentration, and ashfall rate has been statistically derived for various eruption regimes and ash sizes by applying a radar-reflectivity microphysical model, which was previously developed. A prototype algorithm for VARR has been proposed and applied. Starting from measured single-polarization reflectivity, the inversion technique to retrieve ash concentration and fall rate has been based on two cascade steps, namely: 1) a classification of eruption regime and volcanic ash category and 2) estimation of ash concentration and fall rate. The expected accuracy of the VARR algorithm estimates has been evaluated using a synthetic data set. To quantitatively evaluate the ash detectability by weather radars, a sensitivity analysis has been performed by simulating a synthetic ash cloud and varying ash concentration and size as functions of the range. Radar specifications have been taken from typical radar systems at S-, C-, and X-band. An application of the VARR technique has been finally shown, taking into consideration the eruption of the Grímsvötn volcano in Iceland in November 2004. Volume scan data from a Doppler C-band radar, which are located 260 km from the volcano vent, have been processed by means of VARR. Examples of the achievable VARR products have been thoroughly discussed.

The major conclusion of this study is that ground-based weather radars can be successfully used for volcanic ash cloud dynamical monitoring and quantitative retrieval of ash category, concentration, and fall rate. Of course, the expected

accuracy is conditioned by the microphysical assumptions chosen to constrain the inverse problem, even though the Bayesian retrieval approach can easily ingest the knowledge of these uncertainties within the VARR scheme. It is intuitive and has been here demonstrated that the radar detectability of moderate- to low-concentration fine ash is improved if, for the same configuration, the available peak power is higher, the radial resolution is larger, and the observation distance is shorter. X-band radars may represent an optimal solution if they are designed as portable instruments, while a C-band radar network may represent a good compromise for fixed installations.

Further work is needed to assess the VARR potential. Future investigations should be devoted to the analysis of the impact of ash aggregates on microwave radar reflectivity and on the validation of radar estimates of ash amount with ground measurements where available. The last task is not an easy one, as the ash fall is dominated by wind advection and by several complicated microphysical processes [23]. This means that what retrieved within an ash cloud may be not representative of what collected at ground in a given area. Spatial integration of ground-collected and radar-retrieved ash amounts may be considered to carry out a meaningful comparison. The potential of polarimetric weather radars to improve radar estimation of ash clouds should be quantitatively addressed and explored as well.

ACKNOWLEDGMENT

The authors would like to thank R. Hannesen (Selex-Gematronik, Germany) and S. Karlsdóttir and P. Crochet (Iceland Meteorological Office, Iceland) for providing radar data. The contributions of G. Ferrauto and E. Picciotti of CETEMPS (L'Aquila, Italy) are also gratefully acknowledged.

REFERENCES

[1] F. Barberi, G. Macedonio, M. Pareschi, and R. Santacroce, "Mapping the tephra fallout risk: An example from Vesuvius, Italy," *Nature*, vol. 344, no. 6262, pp. 142–144, 1990.

[2] L. Wilson, "Explosive volcanic eruptions—Plinian eruption columns," *Geophys. J. R. Astron. Soc.*, vol. 30, pp. 381–392, 1972.

[3] W. I. Rose, "Scavenging of volcanic aerosol by ash: Atmospheric and volcanological implications," *Geology*, vol. 5, no. 10, pp. 621–624, Oct. 1977.

[4] W. I. Rose, D. Delene, D. Schneider, G. Bluth, A. Krueger, I. Sprod, C. McKee, H. Davies, and G. Ernst, "Ice in the 1994 Rabaul eruption cloud: Implications for volcano hazard and atmospheric effects," *Nature*, vol. 375, no. 6531, pp. 477–479, Jun. 1995.

[5] C. J. Wolfe, I. T. Bjarnason, J. C. VanDecar, and S. C. Solomon, "Seismic structure of the Iceland plume," *Nature*, vol. 385, no. 6613, pp. 245–247, Jan. 1997.

[6] T. P. Miller and T. J. Casadevall, "Volcanic ash hazards to aviation," in *Encyclopaedia of Volcanology*, H. Sigurdsson, Ed. New York: Academic, 2000, pp. 915–930.

[7] W. I. Rose and D. J. Schneider, *Satellite Images Offer Aircraft Protection From Volcanic Ash Clouds*, vol. 77. Pasadena, CA: Electr. Opt. Soc, 1996, pp. 529–532.

[8] G. G. J. Ernst, S. N. Carey, M. I. Bursik, and R. S. J. Sparks, "Sedimentation from turbulent jets and plumes," *J. Geophys. Res.*, vol. 101, no. B3, pp. 5575–5589, Mar. 1996.

[9] W. I. Rose, G. J. S. Bluth, and G. G. J. Ernst, "Integrating retrievals of volcanic cloud characteristics from satellite remote sensors—A summary," *Philos. Trans. R. Soc. London A, Math. Phys. Sci.*, vol. 358, no. 1770, pp. 1585–1606, May 2000.

[10] T. Yu, W. I. Rose, and A. J. Prata, "Atmospheric correction for satellite-based volcanic ash mapping and retrievals using split-window IR data from GOES and AVHRR," *J. Geophys. Res*, vol. 107, no. D16, 4311, Aug. 2002.

[11] S. Wen and W. I. Rose, "Retrieval of sizes and total masses of particles in volcanic clouds using AVHRR bands 4 and 5," *J. Geophys. Res*, vol. 99, no. D3, pp. 5421–5431, Mar. 1994.

[12] N. A. Krotkov, O. Torres, C. Seftor, A. J. Drueger, A. Kostinski, W. I. Rose, G. J. S. Bluth, D. J. Schneider, and S. J. Schaefer, "Comparison of TOMS and AVHRR volcanic ash retrievals from the August 1992 eruption of Mt. Spurr," *Geophys. Res. Lett.*, vol. 26, no. 4, pp. 455–458, Feb. 1999.

[13] G. Dubosclard, R. Cordesses, P. Alard, C. Hervier, M. Coltelli, and J. Kornprobst, "First testing of a volcano Doppler radar (Voldorad) at Mt. Etna," *J. Geophys. Res*, vol. 26, no. 22, pp. 3389–3392, Nov. 1999.

[14] N. Houlié, P. Briole, A. Nercessian, and M. Murakami, "Sounding the plume of the 18 August 2000 eruption of Miyakejima volcano (Japan) using GPS," *Geophys. Res. Lett.*, vol. 32, no. 5, L05302, 2005.

[15] D. M. Harris and W. I. Rose, "Estimating particle sizes, concentrations and total mass of ash in volcanic clouds using weather radar," *J. Geophys. Res*, vol. 88, no. C15, pp. 10 969–10 983, Dec. 1983.

[16] W. I. Rose, A. B. Kostinski, and L. Kelley, "Real time C band radar observations of 1992 eruption clouds from Crater Peak/Spurr Volcano, Alaska," *U.S. Geol. Surv. Bull.*, vol. 2139, no. 12, pp. 19–26, Dec. 1995. (Spurr Eruption, edited by T. Keith).

[17] M. Maki and R. J. Doviak, "Volcanic ash size distribution determined by weather radar," in *Proc. Int. Geosci. and Remote Sens. Symp.*, Sydney, Australia, Jul. 9–13, 2001, pp. 1810–1811.

[18] C. Lacasse, S. Karlsdóttir, G. Larsen, H. Soosalu, W. I. Rose, and G. G. J. Ernst, "Weather radar observations of the Hekla 2000 eruption cloud, Iceland," *Bull. Volcanol.*, vol. 66, no. 5, pp. 457–473, 2004.

[19] M. D. Krohn, L. R. Lemon, and J. Perry, "WSR-88D applications to volcanic ash detection," in *Proc. 1st Nat. NEXRAD Users Conf.*, Norman, OK, Oct. 1994, pp. 333–336.

[20] F. S. Marzano, E. Picciotti, G. Ferrauto, G. Vulpiani, and W. I. Rose, "Volcanic ash remote sensing by ground-based microwave weather radar," in *Proc. General Assem. EGU*, Vienna, Austria, Apr. 25–29, 2005, pp. 212–215. Wien (A).

[21] L. Wilson, "Explosive volcanic eruptions—II: The atmospheric trajectories of pyroclasts," *Geophys. J. R. Astron. Soc.*, vol. 30, no. 2, pp. 381–392, 1972.

[22] K. H. Wohletz, M. F. Sheridan, and W. K. Brown, "Particle size distributions and the sequential fragmentation/transport—Theory applied to volcanic ash," *Geophys. Res. Lett.*, vol. 94, no. B11, pp. 15 703–15 721, 1989.

[23] H.-F. Graf, M. Herzog, J. M. Oberhuber, and C. Textor, "The effect of environmental conditions on volcanic plume rise," *J. Geophys. Res.*, vol. 104, no. 20, pp. 24 309–24 320, Oct. 1999.

[24] G. Veitch and A. W. Woods, "Particle aggregation in volcanic eruption columns," *J. Geophys. Res.*, vol. 106, no. B1, pp. 26 425–26 441, 2001.

[25] F. S. Marzano, G. Vulpiani, and W. I. Rose, "Microphysical characterization of microwave radar reflectivity due to volcanic ash clouds," *IEEE Trans. Geosci. Remote Sens.*, vol. 44, no. 2, pp. 313–327, Feb. 2006.

[26] W. K. Brown and K. H. Wohletz, "Derivation of the Weibull distribution based on physical principles and its connection to the Rosin–Rammler and lognormal distributions," *J. Appl. Phys.*, vol. 78, no. 4, pp. 2758–2763, Aug. 1995.

[27] H. Sauvageot, *Radar Meteorology*. Norwood, MA: Artech House, 1992.

[28] M. Barkat, *Signal Detection and Estimation*. Norwood, MA: Artech House, 1991.

[29] F. S. Marzano, A. Mugnai, G. Panegrossi, N. Pierdicca, E. A. Smith, and J. Turk, "Bayesian estimation of precipitating cloud parameters from combined measurements of spaceborne microwave radiometer and radar," *IEEE Trans. Geosci. Remote Sens.*, vol. 37, no. 1, pp. 596–613, Jan. 1999.

[30] M. T. Gudmundsson, F. Sigmundsson, and H. Bjornsson, "Ice–volcano interaction of the 1996 Gjalp subglacial eruption, Vatnajokull, Iceland," *Nature*, vol. 389, no. 6654, pp. 954–957, 1997.

[31] E. Sturkell, P. Einarsson, F. Sigmundsson, S. Hreinsdottir, and H. Geirsson, "Deformation of Grímsvötn volcano, Iceland: 1998 eruption and subsequent inflation," *Geophys. Res. Lett.*, vol. 30, no. 4, 1182, 2003.

[32] F. Sigmundsson, P. Einarsson, M. Tumi Gudmundsson, T. Hognadottir, A. K. Mortensen, S. Jakobsdottir, M. Roberts, K. Vogfjord, and R. Stefansson, *Eruption of the Grímsvötn volcano, Iceland: Summary of activity November 1–4, 2004,* Nov. 2004. Personal communication.

Frank Silvio Marzano (S'89–M'99–SM'03) received the laurea degree (cum laude) in electrical engineering and the Ph.D. degree in applied electromagnetics from the University of Rome "La Sapienza," Rome, Italy, in 1988 and 1993, respectively.

In 1993, he collaborated with the Institute of Atmospheric Physics, Italian National Research Council (CNR), Rome. From 1994 to 1996, he was with the Italian Space Agency, Rome, as a Postdoctoral Researcher. After being a Lecturer at the University of Perugia, Perugia, Italy, in 1997, he joined the Department of Electrical Engineering and the Centro di Eccellenza in Telerilevamento E Modellistica per la Previsione di Eventi Severi (CETEMPS), University of L'Aquila, L'Aquila, Italy, coordinating the Satellite and Radar Remote Sensing Laboratory. Since 2001, he has been the Italian national delegate for the European COST actions 720 and 280. In 2005, he joined the Department of Electronic Engineering, University of Rome "La Sapienza," where he presently teaches courses on antennas, propagation, and remote sensing. His current research concerns passive and active remote sensing of the atmosphere from ground-based, airborne, and spaceborne platforms, with a particular focus on precipitation using microwave and infrared data, development of inversion methods, radiative transfer modeling of scattering media, and radar meteorology issues. He is also involved in radiopropagation topics in relation to incoherent wave modeling, scintillation prediction, and rain fading analysis along satellite microwave links.

Dr. Marzano received the Young Scientist Award of the XXIV URSI General Assembly in 1993. In 1998, he was the recipient of the ARPAD Award from the Naval Research Laboratory, Washington, DC. Since January 2004, he has been an Associate Editor of IEEE GEOSCIENCE REMOTE SENSING LETTERS.

Stefano Barbieri received the laurea degree in electronic engineering from the University of Rome "La Sapienza," Rome, Italy, in 2005.

In that same year, he joined the Department of Electronic Engineering, University of Rome "La Sapienza," to cooperate on radar remote sensing of volcanic ash clouds.

Gianfranco Vulpiani (M'06) received the laurea and Ph.D. degrees in physics from the University of L'Aquila, L'Aquila, Italy, in 2001 and 2005, respectively.

In 2001, he joined the Department of Physics and the Centro di Eccellenza in Telerilevamento E Modellistica per la Previsione di Eventi Severi (CETEMPS), University of L'Aquila, as a Research Scientist on ground-based radar meteorology with a special focus on C-band applications. In 2004, he was a Visiting Student with Colorado State University (CSU), Fort Collins. Since 2006, he has been with Meteo France as a PostDoctoral Research Scientist in radar meteorology within the European project FLYSAFE. His current research interests are active remote sensing of the atmosphere from ground-based sensors, with a particular focus on development of polarimetric precipitation retrieval techniques and hydrometeors classification.

William I. Rose received the Ph.D. degree in geology from Dartmouth College, Hanover, NH, in 1970.

He is currently a Professor of geology at the Department of Geological Engineering and Sciences, Michigan Technological University, Houghton, where he has worked on volcanic ash research for 34 years. His earliest professional work extended his graduate studies in gas and ash emission studies in Central America and expanded to Indonesia, Washington, Hawaii, and Antarctica. In the 1980s, he began developing an interest in potential aircraft hazards from volcanic clouds, years ahead of any serious scientific efforts toward this issue. With more than 150 published papers on volcanic studies, he has investigated multispecies and regional gas measurements of volcanic emissions, ash/aerosol interactions, aircraft hazards, distal ash fallout patterns, quantitative retrievals of ash particles, and detection of ice in volcanic clouds. He developed the first methodology to use infrared satellite data for quantitative retrievals of ash particles, size, and cloud mass. His groundbreaking work, with his graduate student S. Wen, in 1994 formed the basis for current methods of infrared retrieval of ash particles. His latest work is geared toward merging multisensor retrievals of volcanic clouds, deriving simultaneous data of ash, aerosol, and gas species. He has led efforts to develop new monitoring and analytical tools with a variety of sensors and has published valuable syntheses of remote sensing studies.

Dr. Rose is a member of IAVCEI and a fellow of GSA and AGU.